Oscillatory dynamics of the magnetic moment of a Pt/Co/Ir/Co/Pt synthetic antiferromagnet

R. B. Morgunov,[1,2,3,4,*] A. V. Yurov,[3] V. A. Yurov,[3] A. D. Talantsev,[1,2,5] A. I. Bezverhnii,[1,2] and O. V. Koplak[1,2]

[1]*Institute of Problems of Chemical Physics, 142432, Chernogolovka, Russia*

[2]*Tambov State Technical University, 392000, Tambov, Russia*

[3]*Immanuel Kant Baltic Federal University, 236016, Kaliningrad, Russia*

[4]*I. M. Sechenov First Moscow State Medical University, Ministry of Health of Russia, 119991 Moscow, Russia*

[5]*Department of Emerging Materials Science, DGIST, Daegu, 42988, Republic of Korea*

(Received 9 May 2019; revised manuscript received 24 August 2019; published 3 October 2019)

In this paper, we present a detailed study of the oscillating magnetic relaxation in the synthetic antiferromagnet (SAF) with two ferromagnetic Co layers of different thicknesses separated by an Ir spacer. The four stable magnetic states of the SAF are determined by the mutual alignment of magnetic moments in the layers and are controlled by both the magnetic interlayer exchange interaction and the Zeeman energy. The specific variations in the thicknesses of the layers and/or temperature allow the existence of a "triple point," which corresponds to a coincidence of the critical switching fields for two or three interstate transitions. In this case, two or even three different types of magnetization reversals occur simultaneously and competitively. A nonmonotonic dependence of the domain-wall speed v_{DW} on magnetic field H and an oscillating time dependence of magnetic moment M in a constant magnetic field were observed in a Pt/Co/Ir/Co/Pt synthetic antiferromagnet with perpendicular anisotropy due to interplay between the magnetic nuclei produced by Dzyaloshinskii-Moriya interaction. The proximity of two or three (triple-point) critical fields of SAF switching is the necessary condition for both a nonmonotonic magnetic relaxation and the oscillating time variations of the magnetic moment. The dynamical model describing the interaction and subsequent evolution of the magnetic nuclei demonstrates that this nontrivial magnetic relaxation obeys a simple Schrödinger equation.

DOI: 10.1103/PhysRevB.100.144407

I. INTRODUCTION

The spin valves and synthetic antiferromagnet (SAF) are the simplest devices of spintronics. They consist of two ferromagnetic thin films of different thicknesses (∼1 nm) and a nonmagnetic spacer separating the films (Supplemental Material, Fig. S1 [1]). A deliberately small thickness of the ferromagnetic layers (typically <2 nm) provides the interface with a perpendicular anisotropy which dominates the bulk magnetic anisotropy. Ferromagnetic layers have either a single domain (at linear size ⩽10 nm) or a multidomain (at linear size >100 nm) magnetic structure. Large SAFs are required as a spin-valve platform for the industry of the magnetic sensors applicable in the medical and biology analysis [2,3]. The magnetization reversals and the dynamics of magnetic relaxation affect speed and critical switching field of the spin-valve sensors and SAF structures [4,5]. Although a magnetization reversal in single films is predictable and well described by the Fatuzzo-Labrune model [6,7], the spin valves and SAF structures prove to be a much harder nut to crack. In the case of single films, only two types of the magnetic nuclei with an "up" and "down" magnetic moment exist. The Fatuzzo-Labrune model considers expansion of these nuclei via the domain walls' propagation and a simultaneous multiplication of the nuclei number in the external magnetic field [7,8]. Unlike the single films, the SAF possess an additional exchange coupling between the magnetic layers. This coupling is provided by the Ruderman-Kittel-Kasuya-Yosida exchange interaction oscillating with the distance between the ferromagnetic layers. Depending on the spacer thickness there should exist either ferromagnetic or antiferromagnetic interlayer coupling. In the spin valves, the thickness of the spacer is typically selected to provide maximal negative exchange interaction, i.e., the spin valve is an artificial antiferromagnet or ferrimagnet based on two exchange-coupled layers. In total, there are four types of magnetic nuclei present in the spin valve or SAF (see Fig. 1), in contrast with a single monolayer. There are two "parallel" states (P^+, P^-) and two "antiparallel" (AP^+, AP^-) states. The magnetic relaxation can in principle be monotonic, just like in the ferromagnetic monolayer [5,8]. However, in this paper we are interested in a more complicated nonmonotonic relaxation of magnetic moment [4] and in the quasiperiodical magnetic variations [9] in Pt/Co/Ir/Co/Pt SAF. Long (∼10-min period) magnetic oscillations reported in Ref. [9] have no direct relation to the elegant and very famous oscillations in Co-based SAF under a spin-polarized current [10,11]. The phase portrait of the macroscopic magnetic oscillations plotted in Ref. [9] and the phenomenological features of the process (long oscillation period, spontaneous variations of the magnetic moment, very special requirements to the balanced field, temperature, and layer thickness) were very similar to those of the Belousov-Zhabotinsky reaction [12] in the chemical physics. A remarkable example of long periodical forced oscillations in an alternating magnetic field was found in the SAF structure [13]. The SAF structures

*morgunov2005@yandex.ru

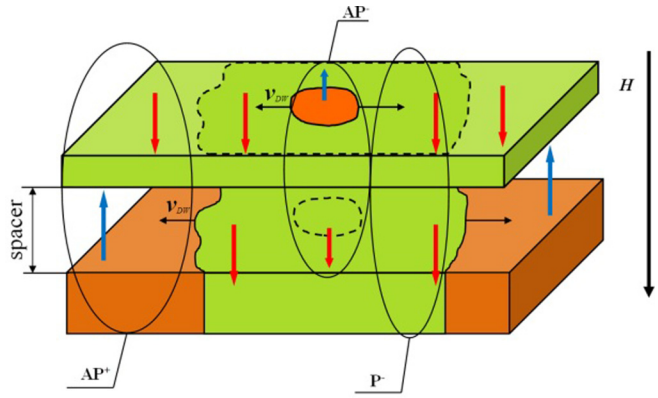

FIG. 1. Sketch of the spin valve, with the denoted areas filled by AP^+, AP^-, and P^- domains.

manifest the following features associated with the nonlinear dynamical systems: temporal oscillations, an excitability, a multistability, a thermoactivated nucleation instead of a reaction-diffusion-driven formation of spatial patterns, and the deterministic chaos corresponding to the Barkhausen noise.

In Ref. [4], the very first fingerprint of an oscillatory magnetic relaxation was identified: a nonmonotonic magnetic relaxation with one extremum which occurs when the system goes through a nonequilibrium state in a constant magnetic field. This naturally led to a question of whether there might exist some other, more complex types of relaxation behavior, particularly the ones that produce magnetic oscillations. The nonmonotonic magnetic relaxation was described in Ref. [4] in a framework of the macrospin theory applied to a number of parallel relaxation processes each related to its own type of magnetic nuclei. Unfortunately, that approach neglected the multidomain structure, the interaction of the magnetic nuclei of four types, the stray fields of the nuclei, Dzyaloshinskii-Moriya interaction (DMI), and many other factors that proved to be too difficult for a quantitative analysis. The experimental microscopic details related to the magnetic nuclei multiplication and interactions were also not included in the model proposed in Ref. [4].

The Co/Ir and Co/Pt interfaces are well known in the literature due to clear evidence of DMI giving rise to noncollinear spin states and producing a complicated dynamics of the domain walls (DWs) [14,15]. An interfacial DMI stabilizes the Néel-type DWs with a clockwise rotational sense [16], the skyrmions [17], and the new topological spin textures such as magnetic radial vortices [18]. A broken spatial symmetry of the interface plays an extremely important role in the current-induced DW propagation process in SAF [19]. In our experiments, we have restricted ourselves to the simplest case of a constant-valued magnetic field. Nevertheless, even with this restriction, we have managed to find a nonmonotonic v_{DW} (H) dependence and to describe it in the frame of a DMI model. The nonmonotonic field dependence of the domain-wall velocity was observed in CoFeB structures [20].

In this paper, we utilize the magneto-optic Kerr effect (MOKE) to analyze the dynamics of generation, expansion, and interaction of the magnetic nuclei during the magnetic relaxation of the SAF in a constant magnetic field. This work was aimed at the analysis of the magnetic nuclei interaction, specifically the field dependence of domain-wall movement and the time dependence of magnetic moment of Pt/Co/Ir/Co/Pt synthetic antiferromagnet. Special efforts were made regarding the analysis of micromagnetic events caused by the constant magnetic field close to the critical fields of the interstate transitions. The work was focused on finding the proper relation between the magnetic nuclei dynamics and the time variations of the sample magnetic moment during the relaxation in a constant magnetic field. The analytic model of spontaneous long-periodic oscillations of the macroscopic magnetic moment was developed.

II. EXPERIMENTAL TECHNIQUE

Multilayered structures $Si/SiO_2/Ta(3\,nm)/Pt(3.2\,nm)/Co(1.1\,nm)/Ir(1.4\,nm)/Co(t_{Co})/Pt(3.2\,nm)$, t_{Co}= 0.60, 0.70, 0.80, and 1.00 nm of 4 × 4-mm^2 sizes were grown by magnetron sputtering at $T = 300$ K (See Supplemental Material, Fig. S1 [1]). The methods of sample preparation and their preliminary chemical, structural, and magnetic attestation were described in Refs. [4,21]. The Ta buffer layer facilitates (111) texture of Co and Pt layers, which provides perpendicular magnetic anisotropy of the synthetic antiferromagnet [21]. The samples satisfied the following conditions:

(1) A perpendicular magnetic anisotropy was provided by hybridization of the 3d orbital moment of Co atoms and the 5d orbital moment of the Pt and Ir atoms. The hybridization enhances an energy splitting between the Co $3d_z{}^2$ and Co $3d_{x^2-y^2}$ orbital states, and it induces the transfer of the spin-polarized charge carriers between the ferromagnetic layers.

(2) The thickness of 1.4 nm of the Ir spacer was selected to provide an antiferromagnetic interlayer exchange coupling comparable with Zeeman energy. This circumstance gives an ample opportunity to switch magnetic stable states of the SAF using the external magnetic field.

Local hysteresis loops and images of the magnetic structure were recorded by Durham Magneto-optics NanoMOKE3 microscope based on the Kerr effect. The microscope was equipped with the rotating sample holder, the quadrupole electromagnet with field range ±1200 Oe, and provided a resolution of magnetic field 0.1 Oe. Scanning laser microscope had magnification up to ×2000 and was equipped with a lens allowing for the measurements of the polar Kerr effect. The sample was mounted in focused laser spots with the diameter of 6 μm. Velocity of the domain walls was determined by the MOKE images. The sample was placed in the magnetic field +800 Oe exceeding the saturation field before each series of the experiments. After the sample saturation the magnetic field was switched down to a negative value. The recording of the series of MOKE images with 0.6-s time interval was started immediately after the stabilization of a value of the magnetic field (a duration of the field stabilization was ∼0.1−0.5 s). The time interval used for plotting the figures was 5–6 s, although intermediate points from the data massive were also available.

The magnetic moment of the sample as a whole and its time dependences were recorded by the MPMS 5XL Quantum Design superconducting quantum interference device (SQUID) magnetometer in $H = 0 - 50$ kOe range in out-of-plane

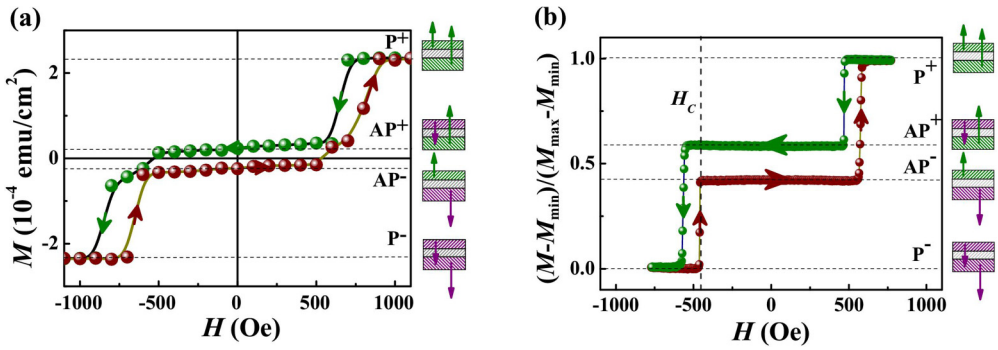

FIG. 2. Hysteresis in Pt(3.2 nm)/Co(1.1 nm)/Ir(1.4 nm)/Co(1 nm)/Pt(3.2 nm) recorded MOKE technique at $T = 300$ K. The magnetic-field sweeping direction is specified by arrows. The horizontal dashed lines indicate stable states, whose orientations are shown in the insets on the right. The field rate is 1.6 kOe/s. Vertical dashed line corresponds to the switching field $H_C = -480$ Oe.

orientation. A diamagnetic contribution of the Si/SiO_2 substrate was subtracted using the linear approximation of the field dependence of a magnetic moment in high magnetic fields (10–50 kOe). A contribution of the transition processes of the magnetometer itself was tested on the Dy_2O_3 reference paramagnetic sample. The amplitude of the intrinsic magnetometer relaxation was negligibly small, $\sim 10^{-3}\%$, relating to a typical change of the magnetic moment of the sample studied in our work (see Supplemental Material, Fig. S2 [1]). A delay of the relaxation measurements of 1.5 min appeared during switching of the magnetic field from a positive to a negative value. We always took into attention this delay whenever the approximation of the time dependences of magnetic moment was used. The samples were mounted in magnetometer with an accuracy $\sim 5°$, which includes the horizontal x component of the external magnetic field applied to the sample.

III. EXPERIMENTAL RESULTS

A. Competition of the AP^- and P^- phases during the magnetic relaxation

Field dependence of the local magnetic moment of the surface area recorded by MOKE technique (Fig. 2) allowed one to identify equilibrium values of the SAF magnetic moment corresponding to different external magnetic fields and to determine critical values of the fields switching between these states. Hysteresis loops recorded by the MOKE technique (Fig. 2) identify four stable states of the SAF (see insets on the left of Fig. 2). Figure 3 demonstrates typical time sequences of the MOKE images recorded in different magnetic fields in the range from -460 to -540 Oe, close to the switching critical field of the free Co layer -480 Oe. In the field -460 Oe, the nuclei of the AP^- phase (white areas) appear on the background of the AP^+ phase (dark area) at $t = 6$ s (Fig. 3, top line). In the constant magnetic field, the expansion of the following AP^- areas takes place. Other processes accompany the magnetization reversal in -530-Oe field. On the background of the starting AP^+ phase (dark area), two phases P^- and AP^- appear simultaneously at $t = 6$ (Fig. 3, bottom line). The P^- phase emerges near surface defects (scratches), while the AP^- phase arises in the exact same areas as observed for the -460-Oe field (Fig. 3, top line). The P^- phase is not an equilibrium state of the SAF in the -530-Oe field. For that reason, at the end of magnetic relaxation at $t = 150$ s the AP^+ and P^- phases end up being suppressed by the AP^- phase equilibrium in this field. In the field -540 Oe, on the background of the AP^+ phase (dark area at $t = 0$) the nuclei of the P^- phase appear near scratches prior to the emergence of the P^- phase (bottom line in Fig. 3). The nonequilibrium P^- nuclei rapidly expand and occupy a large area of the SAF. The AP^- phase starts noticeably later than the P^- phase. Over time the equilibrium AP^- phase expands slowly until it completely replaces the P^- phase at $t = 150$ s.

B. Velocities of the domain boundaries

Linear size D of the few nuclei of the AP^- phase was determined by measurements in the same "horizontal" direction for all sequential frames of time. Series of the linear size dependences on time were recorded in different constant magnetic fields in the $t_{Co} = 1.0$ nm SAF (Fig. 4). The time dependences $D(t)$ of the selected areas of the AP^- phase were close to linear dependences, whose slopes corresponded to the velocities of the domain boundary (Fig. 4). Increasing the absolute value of magnetic field from -433 to

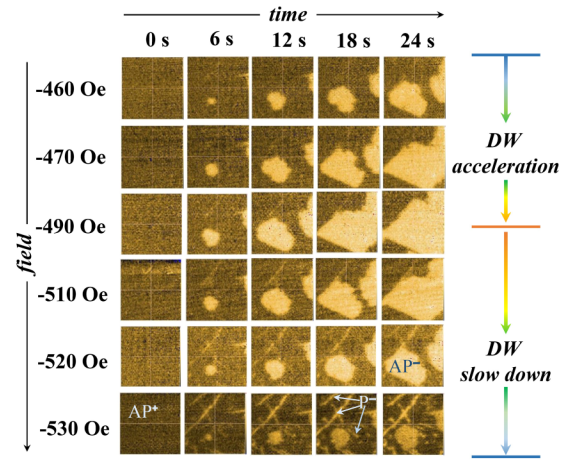

FIG. 3. Sequence of the MOKE images in Pt(3.2 nm)/Co(1.1 nm)/Ir(1.4 nm)/Co(1.0 nm)/Pt(3.2 nm) recorded with 6-s time interval at T = 300 K. Before the recording the sample had been saturated in the +800-Oe field, after which the field has been turned down to one of the values, represented on the left axis.

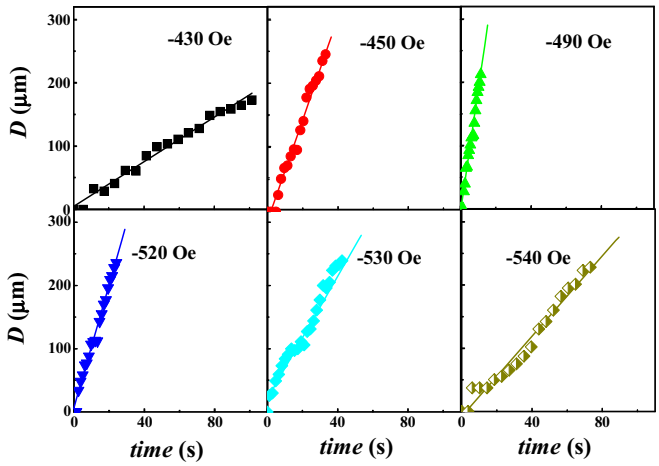

FIG. 4. Field dependences of linear size of the AP^- domain in Pt(3.2 nm)/Co(1.1 nm)/Ir(1.4 nm)/Co(1 nm)/Pt(3.2 nm). Constant magnetic fields of different values were utilized to observe a domain expansion at T = 300 K. The sample was placed in saturated magnetic field +800 Oe before field switching to a new value, indicated in the upper-right corners of corresponding graphs. Pauses between images were $\Delta t = 6$ s.

−490 Oe led to a corresponding increase in the slope of the $D(t)$ dependence; however, subsequent increase in the field, from −490 to −542 Oe, caused the slope to decrease (Fig. 4).

The velocities of the domain boundary $v_{DW}(H) = dD/dt$ of the AP^- phase were calculated by differentiation of the $D(t)$ dependences shown in Fig. 4. Additional analogous dependences for other values of external magnetic fields were used to obtain $v_{DW}(H)$ dependences in Fig. 5. Dependence $v_{DW}(H)$ for the AP^- phase was nonmonotonic and possessing a maximum at magnetic field −490 Oe close to the $H_C =$ −480−Oe switching field from P^- to AP^- state (compare with the vertical dashed line in Fig. 2).

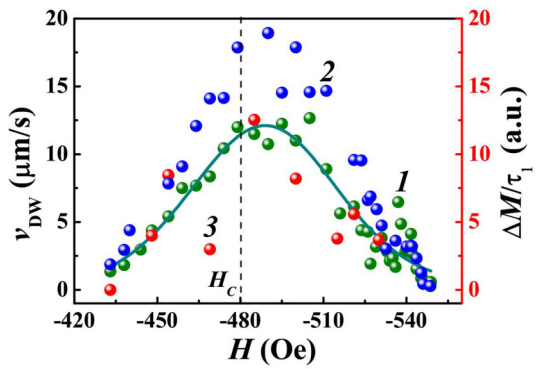

FIG. 5. Field dependences of the AP^- domain boundary speed in Pt(3.2 nm)/Co(1.1 nm)/Ir(1.4 nm)/Co(1.0 nm)/Pt(3.2 nm) sample on magnetic field applied in MOKE microscope at 300 K. The dependences 1, 2 are the measurements of the domain-wall velocity $v_{DW}(H)$ by MOKE for two independent domains. The dependence 3 is the average rate of magnetic moment change $\Delta M/\tau_1(H)$, measured by SQUID magnetometer (see Fig. S3 in Supplemental Material). The solid line is the approximation by formula (9). The vertical dashed line corresponds to switching field $H_C = -480$ Oe.

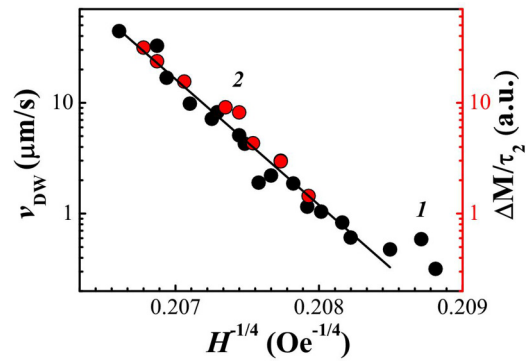

FIG. 6. Field dependence of the velocity of P^- domain expansion, corresponding to a displacement of a P^-/AP^+ domain boundary in Pt(3.2 nm)/Co(1.1 nm)/Ir(1.4 nm)/Co(1.0 nm)/Pt(3.2 nm) at $T =$ 300 K. Curve (1) is a direct measurement of domain-wall velocity $v_{DW}(H)$ by MOKE microscope. Curve (2) is the average relaxation rate $\Delta M/\tau_2(H)$ determined by SQUID. The solid line is the approximation by formula (5).

A dynamics of expansion of the phase P^- in constant magnetic field was analyzed in the same manner (Fig. 6). We used the bottom lines in Fig. 3 to determine the linear size D of the P^- nuclei corresponding to the spots of intermediate brightness (shown by arrows). A domain boundary separating P^- and AP^+ areas was observed, and its velocity v_{DW} was calculated as a derivative of the $D(t)$ dependence for each external field.

Dependence $v_{DW}(H)$ for the AP^- phase was well reproducible for different nuclei (1 and 2 in Fig. 5) as well as for different nuclei of the P^- phase (1 and 2 in Fig. 6). Dependence $v_{DW}(H)$ for the P^- phase was shown to be monotonously decreasing (Fig. 6), in contrast with the $v_{DW}(H)$ dependence for the AP^- phase (Fig. 5). Generation of the P^- phase started at larger absolute values of the magnetic field exceeding −530 Oe in comparison with the AP^- phase.

Field dependences of the velocities measured by MOKE technique (Figs. 5 and 6) can be compared with correspondent field dependences of the average relaxation rate estimated from SQUID data. The nonmonotonic relaxation curves accordingly with Ref. [4] can be decomposed for two exponential functions with time constants τ_1 and τ_2 (Supplemental Material, Fig. S3). An example of the fitting performed to determine time constant τ_1 of $AP^+ \rightarrow AP^-$ transition and τ_2, corresponding to $AP^+ \rightarrow P^-$ transition is shown in Supplemental Material, Fig. S3. The average rate of magnetic moment change determined from SQUID data (Supplemental Material, Fig. S3) was estimated as $\Delta M/\tau_1$ for the AP^- phase (Fig. 5) and $\Delta M/\tau_2$ for the P^- phase (Fig. 6). A good correlation between the accurate velocity determined by a MOKE microscope and the average velocity determined by a SQUID magnetometer was observed, for both the AP^- and P^- phases (Figs. 5 and 6). A presence and relative portions of different phases change with time. At a low absolute value of the field below −440 Oe the AP^- and AP^+ phases can only be observed [Fig. 7(a)]. Starting from −510 Oe the three types of the nuclei AP^+, AP^-, and P^- can be simultaneously observed [Fig. 7(b)]. Starting from −544 Oe, the initial AP^+ phase, reaching a saturation at $t = 0$, disappears, being fully

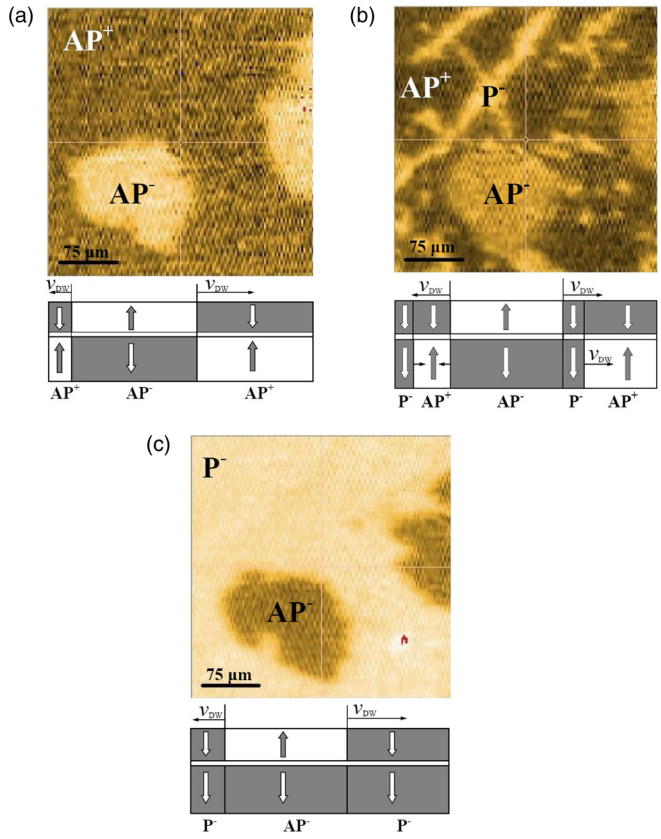

FIG. 7. MOKE images of the domains in Pt(3.2 nm)/Co(1.1 nm)/Ir(1.4 nm)/Co(1.0 nm)/Pt(3.2 nm) at $T = 300$ K in different magnetic fields: (a) $H = -433$ Oe, (b) $H = -532$ Oe, (c) at $H = -544$ Oe.

transformed into a P^- phase [Fig. 7(c)]. Thus, we always observe two of three phases simultaneously.

The thickness of the thin layer t_{Co} affects the field dependence of the velocity of the P^-/AP^+ domain boundary (Fig. 8). Reaching the t_{Co} value close to the thick layer thickness of 1.1 nm effectively alters a monotonic field dependence by changing it into a nonmonotonic one. An equivalence of

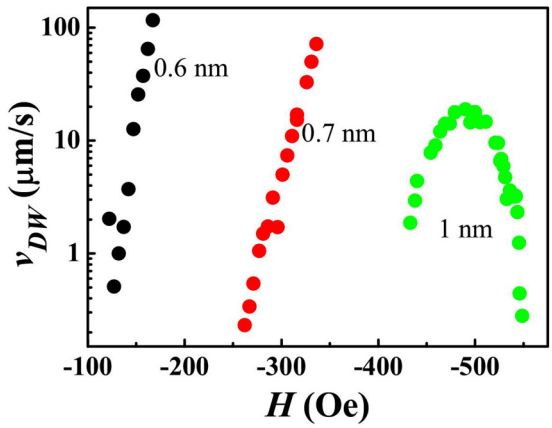

FIG. 8. Field dependences of the domain-wall velocity for the P^-/AP^+ domain boundary in the SAFs with different thicknesses of the thin layer $t_{Co} = 0.6$, 0.7, and 1.0 nm.

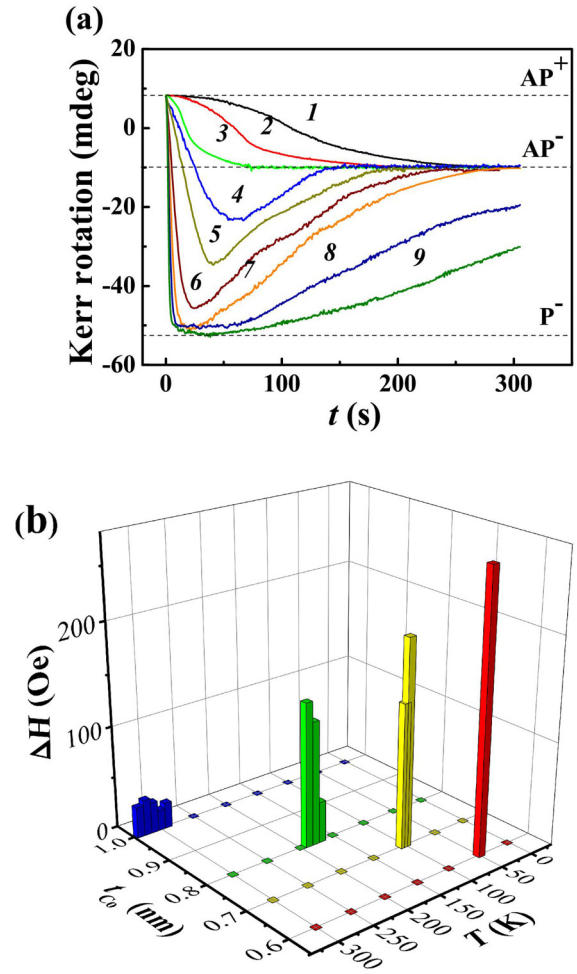

FIG. 9. (a) Magnetic relaxation of the Pt(3.2 nm)/Co(1.1 nm)/Ir(1.4 nm)/Co(1.0 nm)/Pt(3.2 nm) sample measured by MOKE microscope in different magnetic fields: (1) −439 Oe, (2) −444 Oe, (3) −475 Oe, (4) −535 Oe, (5) −537 Oe, (6) −542 Oe, (7) −544 Oe, (8) −546 Oe, (9) −547 Oe at $T = 300$ K. (b) The interval of absolute values of the external magnetic field ΔH, where the nonmonotonic magnetic relaxation is observable, versus the temperature T and the thickness t_{Co} of the Co thin layer. An example of the interval ΔH is presented in Supplemental Material, Fig. S4 [1].

both ferromagnetic layers increases the contribution of the nonlinear interaction between the magnetic nuclei of different types. Nonmonotonic field dependences of the domain-wall velocity take place in those conditions, at which the nonmonotonic time dependences of SAF magnetic moment were observed.

C. Nonmonotonic time dependences of SAF magnetic moment

In Ref. [4], a nonmonotonic time dependence of the magnetic moment of the Pt/Co/Ir/Co/Pt has been described and analyzed in detail. The monotonic relaxation mode from the AP^+ state to the AP^- state [curves 1–3 in Fig. 9(a)] changes to a nonmonotonic relaxation passing first through the P^- states [curves 4–9 in Fig. 9(a)] in constant magnetic field applied during the MOKE recording. An apparent cause for the change in the character of relaxation was a closeness

of the external field value to the critical field of transition (see Fig. 2, vertical line). Such behavior could be expected in a fast sweeping magnetic field, which rapidly changes a nonequilibrium state of the system. Surprisingly, a nonmonotonic relaxation also exists in the constant field. The interval of absolute values of the external magnetic field ΔH, where the nonmonotonic magnetic relaxation is observable, is shown in Fig. 9(b) versus temperature T and thickness t_{Co} of the Co thin layer. Observation of a nonmonotonic magnetic relaxation in a constant magnetic field is only possible in a very narrow range of the temperatures and thin-layer thicknesses [Fig. 9(b)].

The visualization of the interval is shown in Supplemental Material, Fig. S4). One can see a clear direct dependence of the temperatures, permitting for the nonmonotonic relaxation, on the thin-layer thickness [Fig. 9(b)]. The equality of the magnetic anisotropies to the correspondent potential barrier heights of the magnetization reversal of the two layers is, probably, a necessary condition for the nonmonotonic magnetic relaxation observed by both the MOKE (Fig. 9) and the SQUID [Figs. 10(a) and 10(b)] techniques. In this paper, we report a more complicated magnetic relaxation similar to decaying magnetic oscillations [Figs. 10(c) and 10(d)]. At a room temperature the oscillations can be observed in a sample with 1.0-nm Co thin-layer thickness close to the hard Co layer thickness (1.05 nm) [Figs. 10(c) and 10(d)]. Decreasing the temperature has allowed one to observe the oscillations of the magnetic moment in a sample with a smaller thin-layer thickness. Figures 10(c) and 10(d) demonstrate the oscillating behavior in a sample with 0.7-nm thin-layer thickness at 100 K. Cooling bridges the gap between the energies of the magnetic anisotropy of the free and the thick layers [8]. According to data [8], these energies become equal to each other near 100 K, despite the fact that the thicknesses of the layers are quite different. Thus, in order to control the similitude of the layers one can change their temperature instead of their thicknesses. If one of the layers strongly differs from another layer by a magnetic anisotropy, a magnetization reversal of the thick layer effectively "pulls" the magnetic moment of the thin layer to a simplest exponential magnetic relaxation specific for the single layer. A competition between the different types of domains and the suppression of the energetically unfavorable rapidly grown domains P^- create the prerequisites for the oscillating behavior of the magnetic moment and even for bypassing of the equilibrium level a few times depending on the field used [Figs. 10(c) and 10(d)].

IV. DISCUSSION

A. The dynamics of magnetic relaxation

We can propose a straightforward analogy between the magnetic oscillations and one very famous model of oscillations of the concentrations in chemical reactions [12]. Similarly to the famous Belousov-Zhabotinskii reaction the magnetic nuclei can arise, annihilate, and disappear. Since the nonmonotonic and the oscillating time dependences of magnetic moment, which we have described above, all result from the interplay between P^- and AP^- nuclei, we can introduce a dimensionless share of AP^+ nuclei z varying between 0 and 1; a share of P^- nuclei x ($0 \leqslant x \leqslant 1$); a share of the AP^- nuclei y ($0 \leqslant y \leqslant 1$); an efficiency of the P^- nuclei generation

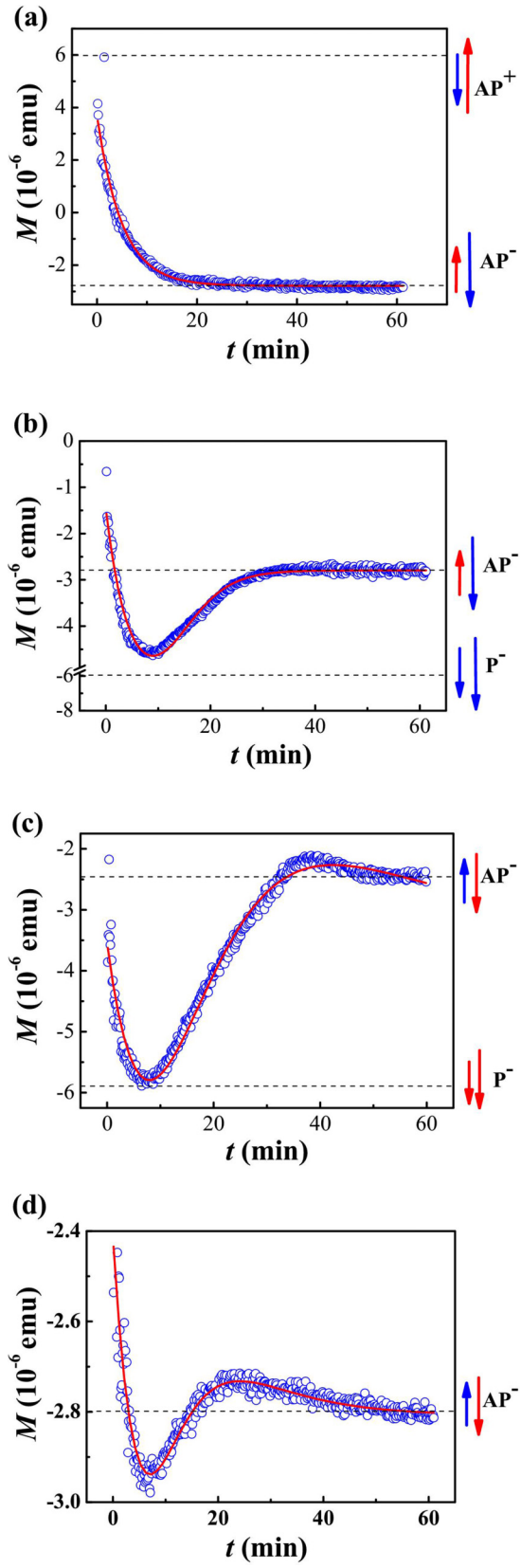

FIG. 10. Some possible types of magnetic relaxation in Pt(3.2 nm)/Co(1.1 nm)/Ir(1.4 nm)/Co(0.7 nm)/Pt(3.2 nm) in magnetic fields −1350 Oe (a), −1360 Oe (b), −1354 Oe (c), −1370 Oe (d) at $T =$ 100 K. The solid lines are exact solutions of the dynamical system (2).

$\alpha(H,T)$ from the AP^+ phase; and an efficiency of the AP^- nuclei generation $\gamma(H,T)$ from the AP^+ phase.

If one assumes the noninteracting AP^+, P^-, and AP^- nuclei, their concentrations will be described by the correspondent dynamical linear system:

$$\frac{dx}{dt} = \alpha z - \beta x$$
$$\frac{dy}{dt} = \gamma z + \beta x$$
$$x + y + z = 1 \tag{1}$$

Initial conditions corresponding to the starting AP^+ state at $t = 0$ are $z = 1$, $x = 0$, $y = 0$. We will consider a SAF with a 1.1-nm thickness of the thick layer and a 0.7-nm thickness of the thin layer. Denoting the saturating magnetic moment of the thick layer by M_{S1}, and that of the thin layer by M_{S2}, one can describe the magnetic relaxation by accounting for the contributions of all three states AP^+, AP^-, P^- : $M(t) = M_{S1}(-x - 0.36y = +z)$. This expression defines, how the x, y, and z shares were used to calculate magnetic moment. The factor 0.36 corresponds to relative difference between magnetic moments of the thick and thin layers $(1.1 - 0.7\,\text{nm})/1.1\,\text{nm} \approx 0.36$. The system (1) predicts a trivial monotonous exponential behavior of the net magnetic moment $M(t) \sim \exp(-t/\tau)$, $\tau = 5\,\text{min}$, involving contributions of all three phases with their weight factors proportional to the correspondent magnetic moments. Approximation of the monotonic relaxation by dynamical system (1) is presented in Fig. 10(a).

The final state of the system is $y(t \to \infty) = 1$, the asymptotic magnetic moment is $-0.4\,M_{S1} = -2.7 \times 10^{-6}\,\text{emu}$ corresponding to the saturation magnetic moment of the thick layer $M_{S1} = -9 \times 10^{-6}\,\text{emu}$ and thin-layer $M_{S2} = 6.3 \times 10^{-6}\,\text{emu}$ [Fig. 10(a)].

Nonmonotonic solutions can be obtained from the nonlinear system, where interaction between the magnetic nuclei accelerates the $P^- \to AP^-$ transition. An additional term should be proportional to the probability δxy of the nuclei approaching each other. The coefficient δ describes the efficiency of the P^--phase absorption by AP^- phase, when these nuclei casually meet each other. Correspondent dynamical system with the same initial conditions $z(0) = 1$, $x(0) = 0$, $y(0) = 0$ is

$$\frac{dx}{dt} = \alpha z - \beta x - \delta xy$$
$$\frac{dy}{dt} = \gamma z + \beta x + \delta xy$$
$$x + y + z = 1 \tag{2}$$

This dynamical model of the magnetic nuclei evolution confirms the possibility of the oscillating magnetic relaxation controlled by an interplay between the nuclei of different types. The exact analytic solution of system (2) as well as its derivation is presented in the Appendix. In particular, the system (2) is proven to be equivalent to the Schrödinger equation, whose regular solutions are shown to be degenerate hypergeometric functions of different orders n (see the Appendix). The resulting time dependences are well described in the case $n = 2$ [Figs. 10(a)–10(c)]. The solution of the system (2) for $n = 1$ is too simple to describe an oscillating magnetic relaxation presented in Figs. 10(c) and 10(d). However, the second order of the solution $n = 2$ gives simultaneous satisfactory approximation of the oscillating magnetic relaxation [solid lines in Figs. 10(c) and 10(d) as well as monotonic [Fig. 10(a)] and nonmonotonic [Fig. 10(b)] dependences. We have derived the following formula for a time dependence of nuclei contributions (see the Appendix):

$$x = \frac{m^2 z(1-z)[(1+2m)z+1]}{m(1+2m)z(mz+2)+m^2+4m+2}$$
$$y = \frac{(1-z)[m(2+3m)z+m^2+4m+2]}{m(1+2m)z(mz+2)+m^2+4m+2}$$
$$z = e^{-\rho t}, \tag{3}$$

and a correspondent dependence of the magnetic moment

$$M = \frac{-3(m^2+4m+2)}{10[m(1+2m)z(mz+2)+m^2+4m+2]} \frac{+z[2(3m^2-23m-13)+mz(20m^2-49m-26-20m(1+2m)z)]}{10[m(1+2m)z(mz+2)+m^2+4m+2]}, \tag{4}$$

with the parameters m and ρ expressed by the initial parameters α, β, γ, δ:

$$\frac{\delta}{\gamma} = m, \quad \frac{\alpha}{\gamma} = \frac{m^2}{1+2m}, \quad \frac{\beta}{\gamma} = \frac{5m+3}{1+2m}, \quad \frac{\rho}{\gamma} = \frac{(1+m)^2}{1+2m}.$$

The asymptotic behavior of (3) and (4) obeys obvious physical conditions corresponding to a final AP^- state of the SAF:

$$\lim_{t\to\infty} x(t) = \lim_{t\to+\infty} z(t) = 0, \lim_{t\to\infty} y(t) = 1.$$

The magnetic moment $M(t \to \infty) = -0.36M_{s1} = -2.7 \times 10^{-6}\,\text{emu}$. In Fig. 10(c) a theoretical curve (solid line) which gives a satisfactory approximation to experimental results (blue circles) is presented. This approximation resulted in $m = 17 \pm 1$; $\rho = 0.1 \pm 0.01\,\text{min}^{-1}$ for $H = -1354\,\text{Oe}$ [Fig. 10(c)]. Corresponding initial parameters of the system (2) are $a = 0.045 \pm 0.005\,\text{min}^{-1}$, $\beta = 0.013 \pm 0.002\,\text{min}^{-1}$, $\gamma = 0.005 \pm 0.0005\,\text{min}^{-1}$, $\delta = 0.09 \pm 0.01\,\text{min}^{-1}$. On the other hand, in a slightly different magnetic field, -1360 Oe, we got $a = 0.074 \pm 0.005\,\text{min}^{-1}$, $\beta = 0.015 \pm 0.002\,\text{min}^{-1}$, $\gamma = 0.006 \pm 0.0005\,\text{min}^{-1}$, $\delta = 0.151 \pm 0.01\,\text{min}^{-1}$ [Fig. 10(b)]. Thus, a small change of the magnetic field practically does not affect frequency β of the $P^+ \to AP^-$ transitions and frequency γ of the transformation of the P^- nuclei to the AP^- nuclei. Magnetic-field change from -1354 Oe until -1360 Oe accelerates frequency of the absorption of the P^- phase by AP^- phase, δ, and frequency of the $AP^+ \to P^-$ transitions, α, up to 1.6 times both. Field dependences of the parameters of the system (2), extracted

from approximation of the nonmonotonic relaxation curves, are presented in the Supplemental Material, Fig. S5 [1]. The reason for the inverse relationship between the values of the parameters and the magnetic field is easy to understand once we recall that as we increase the field, it deviates further and further from the critical value Hc, which corresponds to a simultaneous emergence of all three transitions. These transitions then simply become energetically less favorable the further the field gets from Hc.

One can conclude that for the oscillatory relaxation a strict dominance of the α and δ parameters (shown for oscillatory curves by dashed lines in Supplemental Material, Fig. S5) is something which by all means should emerge. This meshes well with a hypothesis that the growth of a nonequilibrium phase described by α and the probability of the nuclei colliding described by δ should both be significantly high, in order to provide an oscillatory magnetic relaxation. Thus, the field-dependent interaction between the nuclei is necessary to explain the process of oscillating magnetic relaxation.

B. Thermoactivation of the domain walls

In thin ferromagnetic films, there could exist three different modes of domain walls depending on the external magnetic field: a creep in the low field, a depinning in the intermediate field, and a gliding in the strong magnetic field [19]. The creep mode manifests itself as a nonlinear dependence of the domain-wall velocity v_{DW} on the applied magnetic field H. First, we will describe the monotonic field dependence of the P^- domain boundaries. The P^- domains appear in magnetic fields $H < -526$ Oe. A displacement of the domain walls proceeds by jumping from one obstacle to another and is accompanied by the formation of the microsized prominences of the P^- phase (Fig. 7). A field dependence of the thermoactivated velocity of the domain boundary of P^- phase in the creep mode can be described by the following expression [22,23]:

$$v_{DW} = v_0 \exp\left(-\frac{\alpha}{k_B T} H^{-\mu}\right), \tag{5}$$

where v_0 is the characteristic speed, $\alpha = U_C H_d$ is the creep-scaling constant, U_C is the height of the defect-induced pinning-energy barrier, H_d is the depinning field, μ is a universal dynamic exponent equal to 1/4 for a 1D interface moving in a 2D weakly disordered medium [22], k_B is the Boltzmann constant, and T is the temperature. The logarithm of domain-wall velocity $\ln(v)$ was plotted with respect to $H^{-1/4}$ in Fig. 6. It is clear from Fig. 6 that the speed v for each sample follows the creep-scaling law [23]. The parameter α is the most important characteristic here, because there exists a simple relationship between this parameter and the constant of the magnetic anisotropy e in single Co films $\alpha \propto K^{5/8}$. In our experiments, the value $\alpha = 8.6 \times 10^{-10}$ erg Oe$^{-1/4}$ was extracted from the slope of the $\ln(v)(H^{-1/4})$ dependence in Fig. 6. The value thus obtained is compatible with $\alpha = 13.4 \times 10^{-10}$ erg Oe$^{-1/4}$ in single Co film of $t_{Co} = 0.5$-nm thickness determined in Ref. [23]. In Ref. [24], the values of the parameter $\alpha = 0.86 - 9.4 \times 10^{-10}$ erg Oe$^{-1/4}$ were determined for the series of the Pt(4.5 nm)/Co(t_{Co})/Pt(3.5 nm) structures with $t_{Co} = 1 - 3$ nm.

The function $v_{DW}(H)$, which describes the dependence of the AP^- domain boundaries upon the magnetic field, behaves in a more complex and interesting manner (Fig. 5). The movement of the rough boundaries of the AP^- domain phase is characterized by a creep mode in the magnetic fields ranging from -448 to -490 Oe. First, we should distinguish between the stationary and nonstationary modes of the domain-wall displacement. The stationary mode corresponds to a spatial translation of the domain wall with no overall change in the domain boundary structure. In ferromagnets with a perpendicular anisotropy, the stationary mode exists when the magnetic fields do not exceed the critical field $H < H_W$, known as the *Walker field* and corresponding to the *Walker velocity* v_W [25,26]:

$$v_W = 2\pi m_S \Delta \gamma, \tag{6}$$

where m_S is saturation magnetization, Δ is a width of the domain wall, γ is the hyromagnetic ratio. If the magnetic field exceeds the Walker limit $H > H_W$ the movement of the domain wall becomes nonstationary [26], owing to the fact that the demagnetizing field is capped by $4\pi m_S$, so the rate of precession of magnetization as well as the velocity of the domain walls are both bounded from above. For thin single films in the magnetic fields exceeding the Walker limit H_W, the velocity of the domain wall decreases with an increase in a magnetic field. An estimation of the Walker field in a single Co layer of $t_{Co} = 1$-nm thickness gives $H_W = 2200$ Oe [26], and this is about 4–5 times higher than the magnetic field at the maximum of Fig. 5. Furthermore, expression (6) provides us with a theoretical value of the limiting Walker velocity $v_W = 830\,\mu$m/s, which happens to be few orders of value higher, than the determined value for the AP^- domain $v_{DW} = 18\,\mu$m/s. Thus, the nonmonotonic $v_{DW}(H)$ dependence cannot be explained by a mere switch from a stationary to a nonstationary mode upon reaching the Walker limit.

Consider an expansion of the AP^- domain via the absorption of the AP^+ domain (i.e., $AP^+ \rightarrow AP^-$ transition). In this case the displacement of the domain boundary is produced by multiple simultaneous displacements of the domain walls in the thick and thin layers. In contrast, the $AP^+ \rightarrow P^-$ transition corresponds to the P^- domain boundary movement which is restricted to the thick layer, while the thin-layer magnetic moment changes. Similarly, the transition $P^- \rightarrow AP^-$ is accompanied by a movement of the AP^- boundary, which is strictly a thin-layer phenomenon, as the magnetic moment of the thick layer remains constant. The reason for a decrease in the velocity of the domain boundary AP^-/P^- with the absolute value of the magnetic field exceeding -480 Oe lies in the formation of the P^- nuclei, serving as obstacles for the expansion of the AP^- areas. The difference between the full energies (i.e., the sum of Zeeman, exchange, and anisotropy energies) of the AP^- and AP^+ states is greater than the difference between the energies of the AP^- and P^- states. For that reason, a transition from AP^+ to AP^- state is favorable. If the magnetic field drops below -480 Oe, the said difference between the AP^- and P^- states starts diminishing and so does the rate of the $P^- \rightarrow AP^-$ transition. Then, as the field reaches the value $H = -570$ Oe, the P^- state becomes energetically favorable compared to AP^-. In the

absence of the P^- areas at magnetic fields from +480 to −570 Oe, the rate of the $AP^+ \rightarrow AP^-$ transition increases as the magnetic field falls down. The field $H = -480$ Oe, at which the dependence $v_{DW}(H)$ for the $AP^+ \rightarrow AP^-$ transition stops growing and starts to diminish, corresponds to the critical field of the $P^- \rightarrow AP^+$ transition in the hysteresis loop (Fig. 2). The P^- nuclei appear at the field values below the critical transition field near the film defects. The locations of the P^- nuclei form a pattern akin to scratches [Figs. 3 and 7(b)]. The pattern is well reproducible in subsequent magnetic-field cycling.

C. The Dzyaloshinskii-Moriya interaction between the magnetic nuclei

A nucleation of a P^- domain in a thin layer introduces a tilt in the magnetic moment with respect to the normal to the film plane. A nonzero angle between the magnetic moments for the top and bottom layers indicates DMI coupling, which serves as an additional energy barrier for the magnetization reversals. When the AP^- domain wall moves towards the P^- nuclei and attempts to spread over it, the DMI coupling inside the P^- nuclei acts as an additional barrier for $AP^+ \rightarrow AP^-$ transition as well. The energy barrier, associated with DMI, is $E_{DMI} = NDS_tS_b\sin\alpha$, where D is the DMI coupling energy, N is the number of spins present in the activation volume, the S_t and S_b are the coupled spins, correspondingly, in the top and bottom layers, and α is the angle between the directions of local magnetizations of these layers. According to our previous work, the energies of the AP^+ and AP^- states depend on the magnetic moments M_t and M_b and the antiferromagnetic interlayer exchange-coupling energy E_{EX}, as $E_{AP+} = E_{EX} - (M_b - M_t)H$ and $E_{AP^-} = E_{EX} + (M_b - M_t)H$. The pertinent energy barrier for the $AP^+ \rightarrow AP^-$ magnetization reversal would therefore consist of a difference between these two energies, plus the domain pinning energies E_t and E_b in the top and bottom layers, plus the DMI coupling energy E_{DMI}:

$$\Delta E = E_t + E_b + E_{DMI} - 2(M_b - M_t)H.$$

This energy barrier competes with the thermal fluctuation energy k_BT, so the dependence of the velocity of domain wall on the applied magnetic field is

$$v = v_0 \exp\left(-\frac{E_t + E_b + NDS_tS_b \sin\alpha - 2(M_b - M_t)H}{kT}\right). \tag{7}$$

In order to determine how sin (α) depends on the applied magnetic field, we had to analyze the brightness of P^- domains on the MOKE images. Independently on the mechanism of magnetization reversal the dependence of sin α on magnetic field H can be approximated by the equation (Ref. [2])

$$\sin\alpha \sim M/M_S = \left(1 + \exp\left(\frac{H - H_0}{\Delta H}\right)\right)^{-1} \sim \left(1 + \exp\left(\frac{HM_t - E_t}{kT}\right)\right)^{-1}, \tag{8}$$

where H_0 and ΔH are the switching-field mean value and the width of switching-field distribution of the $AP^+ \rightarrow P^-$ magnetization reversal, respectively. From our experiment, $H_0 \sim -490$ Oe and $\Delta H \sim 40$ Oe. Finally, the field dependence of $AP^+ \rightarrow AP^-$ magnetic domain-wall velocity is

$$v = v_0 \exp\left(-\frac{1}{kT}\left(E_t + E_b + NDS_tS_b\left(1 + \exp\left(\frac{HM_t - E_t}{kT}\right)\right)^{-1} - 2(M_b - M_t)H\right)\right). \tag{9}$$

Approximation of the experimental $v(H)$ dependence (Fig. 5) by Eq. (9) yields the following parameters: $(E_t + E_b)/kT = 70$, $NDS_tS_b/kT = 23$. The ratio of the depinning energy of the domain wall to the DMI energy is $r \sim 3$. Therefore, the obtained value of a DMI coupling is comparable with the domain unpinning energy barriers, which lies in a good agreement with the previously collected data in the literature for the DMI coupling in Pt/Co systems [27,28]. Thus, both monotonic and nonmonotonic field dependences of the domain-wall velocity can exist and be observed in the same sample; which type one gets depends solely on the corresponding type of the transition (Supplemental Material, Fig. S6 [1]).

Hitherto, the evidence of the DMI coupling in Ir/Co/Pt and Ta/Co/Pt systems has been proven by several experimental techniques: (1) the modulation of a curvature of the domain boundary under the H_X field, applied in plane, and the H_Z field, applied out of plane [27]; (2) the difference between the domain propagation velocities in the right and the left directions of T junctions [29]; (3) an asymmetric hysteresis loop and the reduction of out-of-plane coercivity under the magnetic field, applied in plane [30]; (4) a shift of the nucleation centers in the bubble domains, either in the right or in the left direction, which depends on the direction of the magnetic field, applied in plane [31]; (5) a reduction in the velocity of a domain wall under field, applied in plane and out of plane [32]; and (6) a shift experienced by the Stokes and anti-Stokes peaks in the Brillouin light-scattering measurements [33]. In our experiment, a reduction in DW velocity corresponding to an increase of the applied z field has been observed. A small projection of the field onto the x axis is not excluded due to a possible ∼5° slope inadvertently introduced during the installation of the sample in the SQUID cell.

Structure of the domain wall can strongly affect their dynamics in magnetic field. The DMI coupling stabilizes Néel type of the domain walls and provides proximity magnetism of the transition metal contacting with ferromagnetic metal in Co/Pt and Co/Ir structures [14]. The domain-wall chirality induced by the DMI at interfaces [34] can influence domain-wall dynamics in our experiments. The DMI can be adjusted to stabilize either left-handed or right-handed Néel walls. The possible contribution of the domain-wall chirality is a factor

requiring following investigation. We cannot clarify its role in this work.

D. Coincidence of critical fields as a reason for magnetic oscillations

The oscillating magnetic relaxation can be explained by a coincidence of the critical magnetic fields for different transitions. The energies of four stable states of the SAF are

$$E_{P+} = -(M_b + M_t) \cdot H + E_{AF}, \tag{10}$$

$$E_{AP+} = -(M_b - M_t) \cdot H - E_{AF}, \tag{11}$$

$$E_{AP-} = (M_b - M_t) \cdot H - E_{AF}, \tag{12}$$

$$E_{P-} = (M_b + M_t) \cdot H + E_{AF}, \tag{13}$$

where M_b and M_t are the magnetic moments of the thick (bottom) and thin (upper) layers, correspondently; E_{AF} is the energy of an interlayer antiferromagnetic coupling. A diagram of the SAF energy versus the magnetic field is presented in Fig. 11. The energies of the P^+, AP^+, AP^-, and P^- states are denoted by solid lines. A transition from the AP^+ to the AP^- state is possible for certain values of the field, provided that the excess of the energy of the AP^+ state over the energy of the AP^- state is greater than the potential barrier $U_{AP+\to AP-}$ of this transition. Since the transition $AP^+ \to AP^-$ corresponds to a remagnetization of the two layers, the barrier $U_{AP+\to AP-}$ is just the sum of the energies of the upper Δ_t and bottom Δ_b layers, i.e., $U_{AP+\to AP-} = \Delta_t + \Delta_b$. The necessary condition of the $AP^+ \to AP^-$ transition is $E_{AP+} \geqslant E_{AP-} + \Delta_t + \Delta_b$. Using the expressions (10)–(13), this condition can be rewritten as

$$-(M_b - M_t)H - E_{AF} = (M_b - M_t)H - E_{AF} + \Delta_t + \Delta_b. \tag{14}$$

In Fig. 11(a), Eq. (14) corresponds to the intersection of the solid-line AP^+ and dashed-line AP^-, which is shifted along the energy axis from the AP^- solid line by the value $\Delta_t + \Delta_b$. Equation (14) gives the critical switching field of the transition from the AP^+ to the AP^- state:

$$H_{AP+\to AP-} = -\frac{1}{2}\frac{\Delta_t + \Delta_b}{M_b - M_t}. \tag{15}$$

The other critical fields corresponding to the rest of transitions $AP^+ \to P^-$ and $P^- \to AP^-$ can be obtained by similar calculations:

$$-(M_b - M_t)H - E_{AF} = (M_b + M_t)H + E_{AF} + \Delta_b \tag{16}$$

The critical field of the $AP^+ \to P^-$ transition is

$$H_{AP+\to P-} = -\frac{2E_{AF} + \Delta_b}{2M_b}. \tag{17}$$

An energy balance for the $P^- \to AP^-$ transition is:

$$(M_b + M_t)H + E_{AF} = (M_b - M_t)H - E_{AF} + \Delta_t. \tag{18}$$

The critical field of the $P^- \to AP^-$ transition is

$$H_{P-\to AP-} = -\frac{2E_{AF} - \Delta_t}{2M_t}. \tag{19}$$

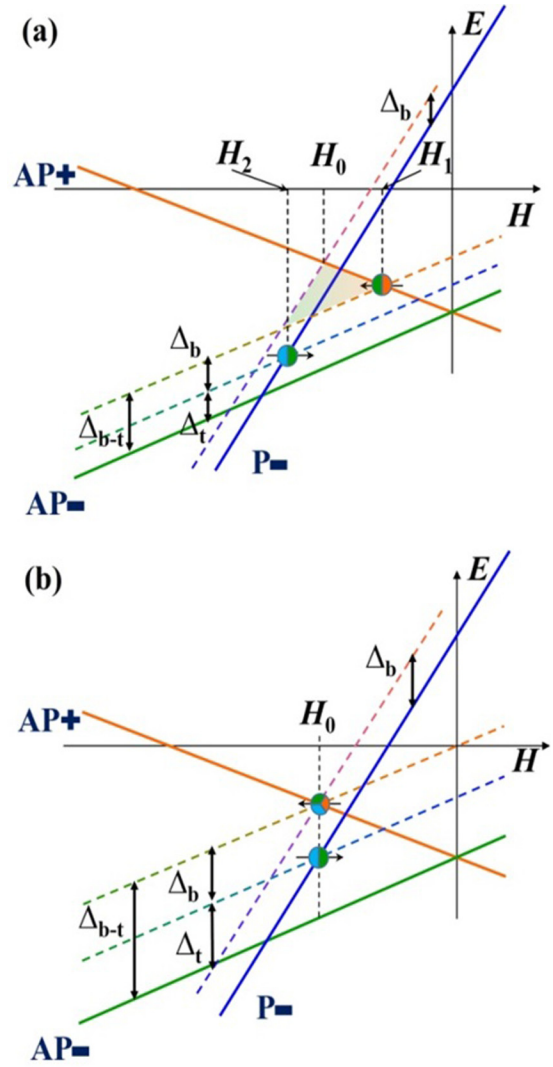

FIG. 11. Energy diagrams versus the magnetic field: (a) the case of anisotropy barriers Δ_b (bottom layer) and Δ_t (top layer) much smaller than interlayer antiferromagnetic coupling E_{AF}. Switching fields for all interstate transitions differ from each other. (b) The case of large anisotropy barriers Δ_t and Δ_b corresponding to a simultaneous presence of both $AP^+ \to AP^-$ and $P^- \to AP^-$ transitions (critical fields of these transitions are situated at the same H value).

We have considered the case when the critical fields of the $AP^+ \to AP^-$ and $AP^+ \to P^-$ transitions coincide. In this case, two kinds of the domains (AP^- and P^-) will appear simultaneously in the same external field. Competition between these two types of the domains results in a suppression of one domain type in favor of the other. A concurrence of the critical transition field of the $AP^+ \to AP^-$ and $P^- \to AP^-$ processes results in two paths of the AP^- state filling: one direct $AP^+ \to AP^-$ transition, or two successive $AP^+ \to P^-$ and $P^- \to AP^-$ transitions [3]. Changes of the magnetic moment of the SAF accompanying mentioned transitions will be nonmonotonic [Fig. 10(b)]. First, the magnetic moment falls down until it reaches its minimal value in the P^- state, after which the magnetic moment grows back again, up to the value corresponding to the AP^- equilibrium state. In this field, the

energy of the P^- state is higher than energy of the AP^- state. Coincidence of the critical fields of the three $AP^+ \rightarrow AP^-$, $AP^+ \rightarrow P^-$, and $P^- \rightarrow AP^-$ transitions (triple point) causes branched pathways of the relaxation between AP^+ and AP^- states. In this case, the AP^- domains grow from two other AP^+ and P^- states simultaneously. This initiates a cascade of the local $AP^+ \rightarrow P^- \rightarrow AP^-$ chain transitions in different areas of the SAF. These transitions are separated in time. Since the $AP^+ \rightarrow P^-$ and $P^- \rightarrow AP^-$ transitions correspond to the opposite signs of the change of the magnetic moment, an independent transformation of those states in different areas of the SAF induces an oscillating behavior in the total magnetic moment of the sample [Figs. 10(c) and 10(d)].

The condition of the coincidence of the critical fields of the above-mentioned transitions can be obtained by setting the corresponding critical fields (15), (17), and (19) equal to each other. In other words, the $AP^+ \rightarrow AP^-$ and $AP^+ \rightarrow P^-$ transitions would appear in the same field if the following condition is satisfied:

$$-\frac{1}{2}\frac{\Delta_t + \Delta_b}{M_b - M_t} = -\frac{2E_{AF} + \Delta_b}{2M_b}. \tag{20}$$

The condition of the simultaneous passing of the $AP^+ \rightarrow P^-$ and $P^- \rightarrow AP^-$ transitions is

$$-\frac{2E_{AF} + \Delta_b}{2M_b} = -\frac{2E_{AF} - \Delta_t}{2M_t}. \tag{21}$$

Conversion of the expressions (20) and (21) results in

$$\Delta_t = 2E_{AF}\left(1 - \frac{M_t}{M_b}\right) - \Delta_b\frac{M_t}{M_b} \tag{22}$$

The condition (22) satisfies both (20) and (21). Thus, the two processes—that of the P^- and AP^- domain formation from the AP^+ state, and the backward magnetization reversal from the AP^+ to AP^- state thought the intermediate P^- state—are energetically equivalent to each other. In Fig. 11(b), energy diagram of the SAF state is shown for the case when the condition (22) is fulfilled. The *C* point corresponds to a transition carried on by two types of the domains. The solid line belonging to the AP^+ state crosses two dashed lines corresponding to the P^- state shifted up by Δ_b value, and the dashed line AP^-, shifted up by $\Delta_b + \Delta_t$ value along energy axis. The *D* point corresponds to the transition $P^- \rightarrow AP^-$ at the same external field as the *C* point.

V. CONCLUSIONS

(1) In $Si/SiO_2/Ta/Pt/Co/Ir/Co/Pt$ synthetic antiferromagnet, magnetic relaxations of different types can be described by the nonlinear dynamical system equivalent to the Schrödinger equation. Regular solutions expressed via the degenerate hypergeometric functions of the second order successfully describe the monotonic exponential relaxation, the nonmonotonic relaxation with a single extremum, and the magnetic relaxation containing two extrema. Field dependences of the extracted parameters indicate a necessity of the term describing the stochastic collisions of the magnetic nuclei of the P^- and AP^- types, in order to explain the observed oscillatory magnetic relaxation.

(2) Tuning of the thin-layer thickness and temperature produces a coincidence of the critical magnetic fields of the two or even three interstate transitions. Double coincidence results in the nonmonotonic magnetic relaxation possessing a single extremum, while the triple point (a coincidence of the three critical fields) causes oscillatory magnetic relaxation.

(3) Nonmonotonic field dependence of the domain-wall velocity was observed in constant magnetic fields $H = -480$ Oe close to the critical field, switching P^- state to the AP^- state. This phenomenon is accompanied by the emergence of the P^- phase and a low velocity of the AP^-/P^- domain boundaries. The origin of the observed nonmonotonic dependence of the magnetic nuclei expansion can be explained by Dzyaloshinskii-Moriya interaction.

(4) A convergence in the thicknesses of two ferromagnetic layers significantly enhances the domain interaction, which results in a nonlinear field dependence of the domain-wall velocity and a nonmonotonic time dependence of the magnetic relaxation manifesting oscillating behavior. An increase of the thin-layer thickness is equivalent to a decrease of the temperature, stimulating the convergence of the magnetic anisotropies of the hard and thin layers to each other, and resulting in nonmonotonic time dependences of the magnetic relaxation.

ACKNOWLEDGMENTS

The work was supported by Ministry of Education and Science of the Russian Federation (Grant No. 3.1992.2017/4.6). We are grateful to Prof. S. Mangin for fruitful discussions and samples presented at our disposal. The study was supported by the "Project for enhancing of competitiveness of leading Russian universities among leading research and educational centers" (5–100). A.B. was supported by Russian Foundation for Basic Research, Grant No. 19-32-90128.

APPENDIX

In order to simplify the system (2) in the main text we sum up first and second equations and then remove the x and y variables altogether via a third equation. This yields a simple first-order separable differential equation:

$$\dot{z} = -(\alpha + \gamma)z,$$

with general solution

$$z = z_0 e^{-\rho t}, \tag{A1}$$

where ρ is a positively defined constant:

$$\rho = \alpha + \gamma.$$

According to (2), this implies that x and y are related to each other in the following fashion:

$$y = 1 - x - z_0 e^{-\rho t}. \tag{A2}$$

Upon substitution of (A1) and (A2) into (2) we end up with an equation this time depending just on x:

$$\dot{x} = \alpha z_0 e^{-\rho t} + [\delta z_0 e^{-\rho t} - \beta - \delta + \delta x]x. \tag{A3}$$

Equation (A3) is a Riccati equation and as such can be linearized by the following change of variable:

$$x(t) = -\frac{1}{\delta}\frac{d}{dt}\ln f(t). \tag{A4}$$

Furthermore, if we additionally rescale the variable $f(t)$ as

$$f(t) = \exp\left[-\frac{1}{2}\left(\sigma t + \frac{\delta z_0}{\rho}e^{-\rho t}\right)\right]V(t),\ \sigma = \beta + \delta,$$

then Eq. (A3) turns into a standard Schrödinger equation for the variable $V(t)$:

$$\frac{\ddot{V}}{V} = \frac{\delta^2}{4}e^{-2\rho t} + \frac{\delta}{2}[\rho - \sigma - 2\alpha]e^{-\rho t} + \frac{1}{4}\sigma^2. \tag{A5}$$

Therefore, the entire problem reduces to finding a regular solution of (A5) which does not vanish for any given $t > 0$ (so that the right-hand side of (A5) remains well defined), and then using it to find x:

$$x(t) = \frac{\sigma}{2\delta} - \frac{z_0}{2}e^{-\rho t} - \frac{1}{\delta}\frac{\dot{V}(t)}{V(t)}. \tag{A6}$$

In order to achieve our goal it would actually be handy to replace a time variable t with an independent variable ξ by the formula

$$\xi = e^{-\rho t}.$$

The Schrödinger equation (A5) would have to be adjusted and turned into

$$V'' + \frac{1}{\xi}V' - \left[a^2 + \frac{ab}{\xi} + \frac{c^2}{\xi^2}\right]V = 0, \tag{A7}$$

where denotes the derivative with respect to the variable ξ, $V = V(\xi)$, and

$$a = \frac{\delta}{2\rho},\ b = 1 - \frac{\sigma + 2\alpha}{\rho},\ c = \frac{\sigma}{2\rho}.$$

Let us now take a closer look at the behavior of the solutions of (A7) for both very small and very large ξ. In order to study the asymptotic behavior of $V(\xi)$ around $\xi = 0$ we shall dispense in with all but the dominant term in square braces in (A5):

$$V'' + \frac{1}{\xi}V' - \frac{c^2}{\xi^2}V = 0.$$

It is easy to see that the general solution of this linear differential equation has the form

$$V(\xi) = c_1\xi^{-c} + c_2\xi^{+c},$$

where c_1 and c_2 are arbitrary real constants. Taking into account that by assumption V cannot be equal to zero (so $c_1 \neq 0$), we conclude that when $\xi \to 0$

$$V \to \xi^{-c}.$$

By a similar argument, one can show that for $\xi \to \infty$

$$V \to e^{\pm a\xi}.$$

Therefore, one can utilize a variable $w(\xi)$, defined as

$$V = \xi^{-c}e^{ka\xi}w(\xi),\ k = \pm 1,$$

which, upon substitution into (A5), further reduces our problem to the equation for the degenerate hypergeometric function:

$$\frac{d^2w(\zeta)}{d\zeta^2} + (1 - 2c - \zeta)\frac{dw(\zeta)}{d\zeta} - a\lambda(k - 2ck - b)w(\zeta) = 0, \tag{A8}$$

where $\zeta = -2ka\xi$. It is advisable to represent the solution of (A8) as

$$V(t) = e^{\sigma t/2}\left[c_1\exp\left(\frac{\delta}{2\rho}e^{-\rho t}\right)w_+(t) + c_2\exp\left(-\frac{\delta}{2\rho}e^{-\rho t}\right)w_-(t)\right]. \tag{A9}$$

Here, as before, c_1 and c_2 are arbitrary real constants, the functions w_+ and w_- are defined as follows:

$$w_+(t) = F\left(\frac{\alpha}{\rho},\ 1 - \frac{\sigma}{\rho},\ -\frac{\delta}{\rho}e^{-\rho t}\right)$$
$$w_-(t) = F\left(1 - \frac{\sigma + \alpha}{\rho},\ 1 - \frac{\sigma}{\rho},\ \frac{\delta}{\rho}e^{-\rho t}\right), \tag{A10}$$

and the function F in (A10) is given by the following convergent series:

$$F(A, B, \zeta) = 1 + \frac{A}{B}\frac{\zeta}{1!} + \frac{A(A+1)}{B(B+1)}\frac{\zeta^2}{2!} + \ldots. \tag{A11}$$

At this step it is very important to note that by itself the convergence of the series in (A11) does not guarantee the regularity of solutions of Eqs. (2). This is due to the fact that for arbitrary c_1 and c_2 the solution (A10) will have at least one zero which will manifest itself as a pole of both $x(t)$ and $y(t)$ [see (A6) and (A2)]. Fortunately, the very form we have chosen for $V(t)$ in (A7) readily gives us the means to overcome this hurdle. For that end, let us choose $c_1 = 0$ [thus getting rid of $w_+(t)$ and the alternating series it represents], and then pick the parameters A and B for $F(A, B, \zeta)$ in $w\_(t)$ [see (A10) and (A11)] as follows:

$$A = -N$$
$$B = 1 - N - \frac{\gamma}{\rho}, \tag{A12}$$

where N is an arbitrary natural number. This particular choice of parameters not only has the benefit of turning the series (A12) into a *finite* positively defined sum—it provides us with infinitely many solutions $V_N(t)$, parametrized by the natural number N:

$$V_N(t) = \exp\left[-\frac{\delta}{2\rho}e^{-\rho t} + \frac{\sigma_N t}{2}\right] \times F\left(-N,\ 1 - N - \frac{\gamma}{\rho},\ \frac{\delta}{\rho}e^{-\rho t}\right), \tag{A13}$$

where

$$\sigma_N = \gamma + N\rho.$$

We conclude this section by providing the explicit formulas for the first three of those positively defined regular solutions:

$$V_1(t) = \exp\left[-\frac{\delta}{2\rho}e^{-\rho t} + \frac{1}{2}(\gamma+\rho)t\right]\left(1+\frac{\delta}{\gamma}e^{-\rho t}\right),$$

$$V_2(t) = \exp\left[-\frac{\delta}{2\rho}e^{-\rho t} + \frac{1}{2}(\gamma+2\rho)t\right]\cdot \times\left(1+\frac{2\delta}{\rho+\gamma}e^{-\rho t} + \frac{\delta^2}{\gamma(\rho+\gamma)}e^{-2\rho t}\right),$$

$$V_3(t) = \exp\left[-\frac{\delta}{2\rho}e^{-\rho t} + \frac{1}{2}(\gamma+3\rho)t\right]\cdot \times\left(1+\frac{3\delta}{2\rho+\gamma}e^{-\rho t} + \frac{3\delta^2}{(2\rho+\gamma)(\rho+\gamma)} \times e^{-2\rho t} + \frac{\delta^3}{(2\rho+\gamma)(\rho+\gamma)\gamma}e^{-3\rho t}\right).$$

These solutions are for $n = 2$ formulas presented in the main text.

[1] See Supplemental Material at http://link.aps.org/supplemental/10.1103/PhysRevB.100.144407 for six more figures related to the experiment.

[2] P. P. Freitas, F. A. Cardoso, V. C. Martins, S. A. M. Martins, J. Loureiro, J. Amaral, R. C. Chaves, S. Cardoso, L. P. Fonseca, A. M. Sebastiano, M. Pannetier-Lecoeure, and C. Fermon, Lab Chip **12**, 546 (2012).

[3] G. Li, S. Sun, R. J. Wilson, R. L. White, N. Pourmand, and S. X. Wang, Sens. Actuators A: Phys. **126**, 98 (2006).

[4] T. Fache, H. S. Tarazona, J. Liu, G. L'vova, M. J. Applegate, J. C. Rojas-Sanchez, S. Petit-Watelot, C. V. Landauro, J. Quispe-Marcatoma, R. Morgunov, C. H. W. Barnes, and S. Mangin, Phys. Rev. B **98**, 064410 (2018).

[5] A. Talantsev, Y. Lu, T. Fache, M. Lavanant, A. Hamadeh, A. Aristov, O. Koplak, R. Morgunov, and S. Mangin, J. Phys.: Condens. Matter **30**, 135804 (2018).

[6] A. Kirilyuk, J. Ferre, V. Grolier, J. P. Jamet, and D. Renard, J. Magn. Magn. Mater. **171**, 45 (1997).

[7] M. Labrune, S. Andrieu, F. Rio, and P. Bernstein, J. Magn. Magn. Mater. **80**, 211 (1989).

[8] R. B. Morgunov, G. L. L'vova, A. D. Talantsev, O. V. Koplak, T. Fache, and S. Mangin, J. Magn. Magn. Mater. **459**, 33 (2018).

[9] R. B. Morgunov and G. L. L'vova, JETP Lett. **108**, 137 (2018).

[10] S. I. Kiselev, J. C. Sankey, I. N. Krivorotov, N. C. Emley, R. J. Schoelkopf, R. A. Buhrman, and D. C. Ralph, Nature (London) **425**, 380 (2003).

[11] J. C. Slonczewski, J. Magn. Magn. Mater. **159**, L1 (1996).

[12] R. J. Field, Mod. Phys. Lett. B **29**, 1530015 (2015).

[13] L. Thomas, J. Luning, A. Scholl, F. Nolting, S. Anders, J. Stohr, and S. S. P. Parkin, Phys. Rev. Lett. **84**, 3462 (2000).

[14] R. M. Rowan-Robinson, A. A. Stashkevich, Y. Roussigne, M. Belmeguenai, S.-M. Cherif, A. Thiaville, T. P. A. Hase, A. T. Hindmarch, and D. Atkinson, Sci. Rep. **7**, 16835 (2017).

[15] G. Ziemys, V. Ahrens, S. Mendisch, G. Csaba, and M. Becherer, AIP Adv. **8**, 056310 (2018).

[16] M. Perini, S. Meyer, B. Dupe, S. von Malottki, A. Kubetzka, K. von Bergmann, R. Wiesendanger, and S. Heinze, Phys. Rev. B **97**, 184425 (2018).

[17] C. Moreau-Luchaire, C. Moutafis, N. Reyren, J. Sampaio, C. A. F. Vaz, N. Van Horne, K. Bouzehouane, K. Garcia, C. Deranlot, P. Warnicke, P. Wohlhuter, J.-M. George, M. Weigand, J. Raabe, V. Cros, and A. Fert, Nat. Nanotechnol. **11**, 444 (2016).

[18] D. Khadka, S. Karayev, and S. X. Huang, J. Appl. Phys. **123**, 123905 (2018).

[19] Y. Ishikuro, M. Kawaguchi, N. Kato, Y. Lau, and M. Hayashi, Phys. Rev. B **99**, 134421 (2019).

[20] A. Hamadeh, P. Pirro, J.-P. Adam, Y. Lu, M. Hehn, S. Petit Watelot, and S. Mangin, Appl. Phys. Lett. **111**, 022407 (2017).

[21] S. Emori and G. S. D. Beach. J. Appl. Phys. **110**, 033919 (2011).

[22] F. Cayssol, D. Ravelosona, C. Chappert, J. Ferré, and J. P. Jamet, Phys. Rev. Lett. **92**, 107202 (2004).

[23] S. Lemerle, J. Ferre, C. Chappert, V. Mathet, T. Giamarchi, and P. Le Doussal, Phys. Rev. Lett. **80**, 849 (1998).

[24] D. H. Kim, S.-C. Yoo, D.-Y. Kim, K.-W. Moon, S.-G. Je, C.-G. Choe, B.-C. Min, and S.-B. Choe, Appl. Phys. Lett. **104**, 142410 (2014).

[25] N. L. Schryer and L. R. Walker, J. Appl. Phys. **45**, 5406 (1974).

[26] P. J. Metaxas, J. P. Jamet, A. Mougin, M. Cormier, J. Ferré, V. Baltz, B. Rodmacq, B. Dieny, and R. L. Stamps, Phys. Rev. Lett. **99**, 217208 (2007).

[27] Y. Yoshimura, K.-J. Kim, T. Taniguchi, T. Tono, K. Ueda, R. Hiramatsu, T. Moriyama, K. Yamada, Y. Nakatani, and T. Ono, Nat. Phys. **12**, 157 (2016).

[28] A. Cao, X. Zhang, B. Koopmans, Sh. Peng, Yu. Zhang, Z. Wang, S. Yan, H. Yang, and W. Zhao, Nanoscale **10**, 12062 (2018).

[29] J. Kwon, H. Hwang, J. Hong, and C. You, Sci. Rep. **8**, 18035 (2018).

[30] D. Han, N. Kim, J. Kim, Y. Yin, J. Koo, J. Cho, S. Lee, M. Klaui, H. J. M. Swagten, B. Koopmans, and C. You, Nano Lett. **16**, 4438 (2016).

[31] A. Hrabec, N. A. Porter, A. Wells, M. J. Benitez, G. Burnell, S. McVitie, D. McGrouther, T. A. Moore, and C. H. Marrows, Phys. Rev. B **90**, 020402(R) (2014).

[32] F. Ajejas, V. Krizakova, D. Chaves, J. Vogel, P. Perna, R. Guerrero, A. Gudin, J. Camarero, and S. Pizzini, Appl. Phys. Lett. **111**, 202402 (2017).

[33] J. Cho, N. Kim, S. Lee, J. Kim, R. Lavrijsen, A. Solignac, Y. Yin, D. Han, N. J. J. van Hoof, H. J. M. Swagten, B. Koopmans, and C. You, Nat. Commun. **6**, 7635 (2015).

[34] G. Chen, T. Ma, A. T. N'Diaye, H. Kwon, C. Won, Y. Wu, and A. K. Schmid, Nat. Commun. **4**, 2671(2013).